NANO · MICRO small
www.small-journal.com

An Electroactive and Self-Assembling Bio-Ink, based on Protein-Stabilized Nanoclusters and Graphene, for the Manufacture of Fully Inkjet-Printed Paper-Based Analytical Devices

Alessandro Silvestri, Silvia Vázquez-Díaz, Giuseppe Misia, Fabrizio Poletti, Rocío López-Domene, Valeri Pavlov, Chiara Zanardi, Aitziber L. Cortajarena,* and Maurizio Prato**

Hundreds of new electrochemical sensors are reported in literature every year. However, only a few of them makes it to the market. Manufacturability, or rather the lack of it, is the parameter that dictates if new sensing technologies will remain forever in the laboratory in which they are conceived. Inkjet printing is a low-cost and versatile technique that can facilitate the transfer of nanomaterial-based sensors to the market. Herein, an electroactive and self-assembling inkjet-printable ink based on protein-nanomaterial composites and exfoliated graphene is reported. The consensus tetratricopeptide proteins (CTPRs), used to formulate this ink, are engineered to template and coordinate electroactive metallic nanoclusters (NCs), and to self-assemble upon drying, forming stable films. The authors demonstrate that, by incorporating graphene in the ink formulation, it is possible to dramatically improve the electrocatalytic properties of the ink, obtaining an efficient hybrid material for hydrogen peroxide (H_2O_2) detection. Using this bio-ink, the authors manufactured disposable and environmentally sustainable electrochemical paper-based analytical devices (ePADs) to detect H_2O_2, outperforming commercial screen-printed platforms. Furthermore, it is demonstrated that oxidoreductase enzymes can be included in the formulation, to fully inkjet-print enzymatic amperometric biosensors ready to use.

1. Introduction

The willingness to improve the standards of healthcare, food safety, and environmental sustainability all over the globe is the leading impulse behind the development of disposable biosensors.[1] In particular, disposable electrochemical sensors can play a central role in democratizing sensing, as they are sensitive, cost-effective, portable, and easy-to-use platforms. Nowadays, millions of people have no access to clinical or environmental laboratories. Where resources are limited, low-cost and easy-to-use analytical platforms designed for short-term or single-use applications, could play a significant role. Undeniably, the most important factor defining disposability is economic efficiency: high-throughput fabrication, low-cost raw materials, and manufacturing processes are fundamental aspects in the design of single-use devices. Luckily, in recent years, increasing attention is being

A. Silvestri, S. Vázquez-Díaz, R. López-Domene, V. Pavlov, A. L. Cortajarena, M. Prato
Center for Cooperative Research in Biomaterials (CIC BiomaGUNE)
Basque Research and Technology Alliance (BRTA)
Donostia-San Sebastián 20014, Spain
E-mail: asilvestri@cicbiomagune.es; alcortajarena@cicbiomagune.es; mprato@cicbiomagune.es

G. Misia, M. Prato
Department of Chemical and Pharmaceutical Sciences
Universitá Degli Studi di Trieste
Trieste 34127, Italy

The ORCID identification number(s) for the author(s) of this article can be found under https://doi.org/10.1002/smll.202300163.

DOI: 10.1002/smll.202300163

F. Poletti
Department of Chemical and Geological Sciences
University of Modena and Reggio Emilia
Modena 41125, Italy

R. López-Domene
POLYMAT and Applied Chemistry Department
Faculty of Chemistry
University of the Basque Country UPV/EHU
Donostia-San Sebastián 20018, Spain

C. Zanardi
Department of molecular sciences and nanosystems
Ca' Foscari University of Venice
Venezia 30170, Italy

C. Zanardi
Institute of Organic Synthesis and Photoreactivity
National Research Council of Italy
Bologna 40129, Italy

A. L. Cortajarena, M. Prato
Ikerbasque
Basque Foundation for Science
Bilbao 48009, Spain

paid to the environmental sustainability and ecological footprint of these devices, both during their manufacturing process and after their use.[2,3] Once thrown away, electronics contribute to the increasing problem of e-waste, constituting the fastest increasing waste source, with less than 40% of refuse recycled; therefore, their responsible production and disposal are necessary.

The application of novel printing technologies is a promising solution to answer the economic and environmental challenges affecting the manufacturing of disposable electronics with the potential to overstage conventional solid-state semiconductor technology. Inkjet printing, historically belonging to the graphic art sector, is a well-established deposition technique that is currently being reinvented to manufacture low-cost sensors.[4] Inkjet printing does not require expensive infrastructures (e.g., clean rooms or controlled environments) and can be easily integrated into industrial production lines with a minimum investment. Moreover, it is a completely digital technique, which means that it does not require the use of physical aids, such as photomasks or stencils. Therefore, the electrode design can be easily changed with computer-aided design (CAD) programs at little costs. Furthermore, this technique requires reduced amounts of electroactive/conductive materials if compared to screen printing, further cutting down the electrode production costs.[4]

Several are the substrates compatible with inkjet printing; rigid traditional substrates (e.g., silicon, glass, ceramics) and flexible materials such as synthetic polymers (e.g., polystyrene, polyethylene terephthalate, polymethyl methacrylate, polytetrafluoroethylene) and cellulose-based materials (e.g., paper, nitrocellulose, nano-cellulose, cellophane) are the most diffused ones.[5] Among all, paper is particularly interesting for disposable sensors as it comprises several desirable qualities such as low cost, flexibility, biodegradability, recyclability, and biocompatibility.[6] In addition, it may impart special characteristics to the sensor device, such as the remotion of specific interferents, pre-concentration of the analyte, or support for specific reactants useful for analytical detection.[7] Due to the rising environmental consciousness, inks with a reduced ecological footprint are sought-after nowadays.[8,9] Most conductive ink formulations are based on Ag, Au, and Cu, exploiting their excellent metallic and conductive properties. With the aim of avoiding or at least reducing the use of these precious metals, carbon nanomaterials (e.g., graphite, graphene, nanotubes) have been investigated as a low-cost and eco-friendly alternative.[8,10,11] With the same optic, several efforts are focused on the development of water-based inks to replace solvent-based ones, reducing the release of volatile organic compounds.[9,12–14] However, there is a bottleneck affecting the development of water-based inks, namely the strict rheological conditions that inkjet printing imposes. In fact, water does not match the optimal values of viscosity and surface tension required by this printing technique.[12,13,15,16] In recent years, inkjet-printable water-based conductive inks started flourishing, however, their application in electrochemical sensing is still limited to a few examples.[17–20]

While several conductive inkjet printable solutions, based on graphene and metallic nanoparticles, have been proposed in the literature,[21] the first examples of inks able to respond to a specific stimulus recently started to appear.[21,22] Most of the reported nanomaterial-based inks are responsive to physical stimuli, such as pressure,[23–25] temperature,[26,27] or light.[28,29] The inks responsive to chemical stimuli are typically limited to gas,[30,31] pH,[32,33] and humidity[32,34] detection. To date, responsiveness to more complex chemical stimuli, such as clinically or environmentally relevant analytes, is typically achieved by post-functionalization of the printed devices.[22]

Therefore, the discovery, development, and implementation of processable electroactive materials, able to transduce chemical or biological stimuli into an analytical signal, is pivotal for the development of increasingly efficient printed electrodes.[12] Herein, we propose an inkjet printable hybrid material, able to perform all the functions required for an electrochemical sensor: immobilization and stabilization of the bioreceptors, recognition of the analyte, transduction, and amplification of the signal. The novelty of this work resides in the multifunctionality of the ink which allows the detection of non-electroactive analytes without the need for post-functionalization of the analytical platform. The proposed ink is based on a particular class of engineered proteins called consensus tetratricopeptide proteins (CTPR). These proteins provide several advantages for the design of biosensors: i) rod-like shaped long CTPR proteins, which present a right-handed super-helical structure,[35] upon drying, can form stable and ordered films exploiting side-to-side and head-to-tail inter-molecular interactions;[36,37] ii) these films can be used as efficient support to occlude and immobilize both enzymes and nanomaterials;[38–40] iii) CTPR proteins can act as templates to produce dimensionally controlled metallic nanoclusters[41–43] with redox properties.[44] In this work, we exploit the properties of CTPR-coordinated metallic nanoclusters to form a protein film in which it is possible to entrap graphene and an oxidoreductase enzyme. We demonstrate that the presence of graphene creates a synergistic effect enhancing the electrocatalytic properties of the metallic clusters for both H_2O_2 reduction and oxidation, reducing in this way the amount of metal required to obtain a highly sensitive biosensor. The obtained electroactive hybrid material is used to formulate a water-based inkjet-printable ink. Thanks to its marked electrocatalytic properties, the bio-ink will be used in combination with commercially available graphite and silver water-based inks to manufacture fully inkjet-printed electrochemical paper-based analytical devices (ePADs) for the realization of enzymatic sensors exploiting oxidoreductase enzymes. In this respect, we demonstrate that glucose oxidase can be incorporated into the ink formulation to allow glucose detection.

2. Results and Discussion

2.1. Identification of the Best Performing Electrocatalytic Material

2.1.1. Synthesis of the CTPR Coordinated Metal Nanoclusters

Metal nanoclusters (NCs) are emerging as key components in sensing applications, due to the electron quantum confinement and other outstanding characteristics imparted by their ultra-small size, which is comparable with the dimension of the Fermi wavelength of electrons.[45] These attributes confer

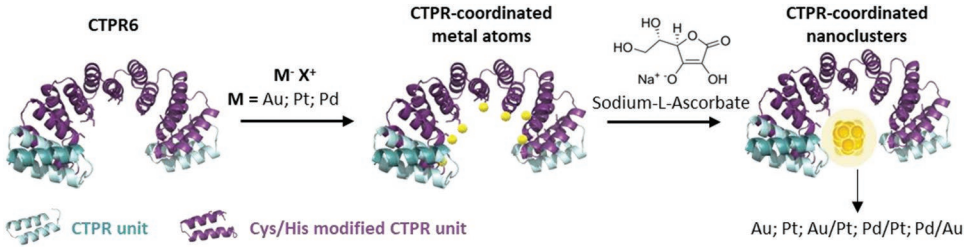

Figure 1. Synthetic scheme of the CTPR-coordinated metallic nanoclusters.

unusual optical and electronic properties to the NCs, that make them suitable candidates for sensing, catalysis, biolabeling, and imaging.[46] By controlling their size, shape, and composition, the redox potentials of metallic NCs can be tuned to operate as effective electron transfer mediators for electrocatalysis.[47]

In the current study, we explored the potential of various CTPR-coordinated metallic NCs to be used as electrocatalysts. CTPR proteins with the capability to template and stabilize metallic NCs are used. In particular, CTPR6 proteins in which the four internal CTPR units are modified with four histidines ($C6_{His16}$) or cysteines ($C6_{Cys16}$) are employed (**Figure 1**), as reported in previous investigations.[41] CTPR6 was chosen as a template for the stabilization of the metal NCs as provides a good compromise between a stable protein scaffold and large enough NCs that do not display high polydispersity. In fact, previous works of the group proved that augmenting the number of module repeats increases the stability of the CTPR proteins,[48,49] while a further increase in the number of modules has a positive effect on the nanomaterial size but a counterproductive effect on the polydispersity of the NCs.[50]

The presence of these two amino acids allows the coordination of diverse metals, creating a library of monometallic and bimetallic NCS: namely histidine-coordinated platinum clusters (PtNC@$C6_{His16}$), cysteine-coordinated platinum clusters (PtNC@$C6_{Cys16}$), cysteine-coordinated gold clusters (AuNC@$C6_{Cys16}$), histidine-coordinated platinum and gold (10:1) clusters (PtAuNC@$C6_{His16}$), cysteine-coordinated platinum and gold (10:1) clusters (PtAuNC@$C6_{Cys16}$), histidine-coordinated palladium and gold (10:1) clusters (PdAuNC@$C6_{His16}$), cysteine-coordinated palladium and gold (10:1) clusters (PdAuNC@$C6_{Cys16}$), histidine-coordinated platinum and palladium (1:1) clusters (PtPdNC@$C6_{His16}$) and cysteine-coordinated platinum and palladium (1:1) clusters (PtPdNC@$C6_{Cys16}$). Au, Pt, and Pd metals were chosen for their well-known catalytic activity, being therefore good starting points for our investigation.[47] The NCs were synthesized by incubating the respective CTPR-coordinating proteins with different metal salts ratios, and consequently reducing the salts with sodium ascorbate (Figure 1). The dimensions and morphology of the NCs@C6 were investigated through transmission electron microscopy (TEM, Figure S1, Supporting Information). The sizes of the nanoclusters, obtained from the TEM images, were consistent with previously reported NCs@C6.[42] Besides, the TEM images verified the absence of larger nanoparticles or NCs aggregates in the colloidal solution, demonstrating that both $C6_{His16}$ and $C6_{Cys16}$ are effective templating and stabilizing agents for the nanoclusters. The metal content and the metal ratio in the bimetallic NCs were studied by inductively coupled plasma mass spectroscopy (ICP-MS) (Table S1, Supporting Information), while the protein concentration was calculated from bicinchoninic acid colorimetric assay (BCA). From these measurements, the protein/metal and metal/metal ratios (for bimetallic NCs) were determined (Table S1, Supporting Information). ICP-MS analysis confirmed the particle composition and the integration of the two metals in the bimetallic NC. Furthermore, ICP-MS analysis proved that NCs metals-ratio can be tuned modulating the equivalents of salts used during the synthesis, even if some deviations from the nominal values can be observed.

2.1.2. Study of the Electrocatalytic Activity of CTPR-Coordinated Metal NCs

Next, we investigated the electrocatalytic activity of the NCs@C6 towards the electrochemical reduction and oxidation of H_2O_2, analyzing the effect of the metallic composition and of the coordination chemistry on the properties of the NCs.

H_2O_2 is an important compound, involved in the exchange of electrons in several biological processes. For instance, H_2O_2 is produced as a by-product of oxidoreductase-catalyzed reactions, which are widely used in biosensing.[51] Furthermore, H_2O_2 plays a crucial role in pharmaceutical and clinical applications. This molecule is acknowledged as a key risk factor in the progression of several pathologies, such as Alzheimer´s and Parkinson´s diseases, atherosclerosis, cancer, or renal failures.[52,53] Therefore, the development of selective and sensitive technologies for H_2O_2 detection is pivotal for numerous biomedical applications.

The electrocatalytic performance of the various metallic systems synthesized was investigated employing a conventional three-electrode cell configuration, where a platinum mesh was used as a counter electrode (CE), a silver/silver chloride (Ag/AgCl) electrode saturated in potassium chloride (KCl) as a reference electrode (RE) and a glassy carbon electrode (GC, 3 mm diameter) as the working electrode (WE). The surface of the WE was modified by drop-casting the solutions of NCs@C6 and letting them dry. A thin layer of Nafion was deposited on top to prevent mechanical detachment of the electrocatalytic material. The electrochemical tests were carried out using cyclic voltammetry (CV); experiments were performed in the absence and in the presence of 1 mM H_2O_2, using 0.1 M phosphate buffer (PBS, pH 7.0) and 0.1 M KCl as the supporting electrolyte (Figures S2 and S3, Supporting Information). To unravel the effect due to the interference of the electrochemical reduction of oxygen dissolved in this solution, these preliminary experiments were performed under an argon atmosphere. The

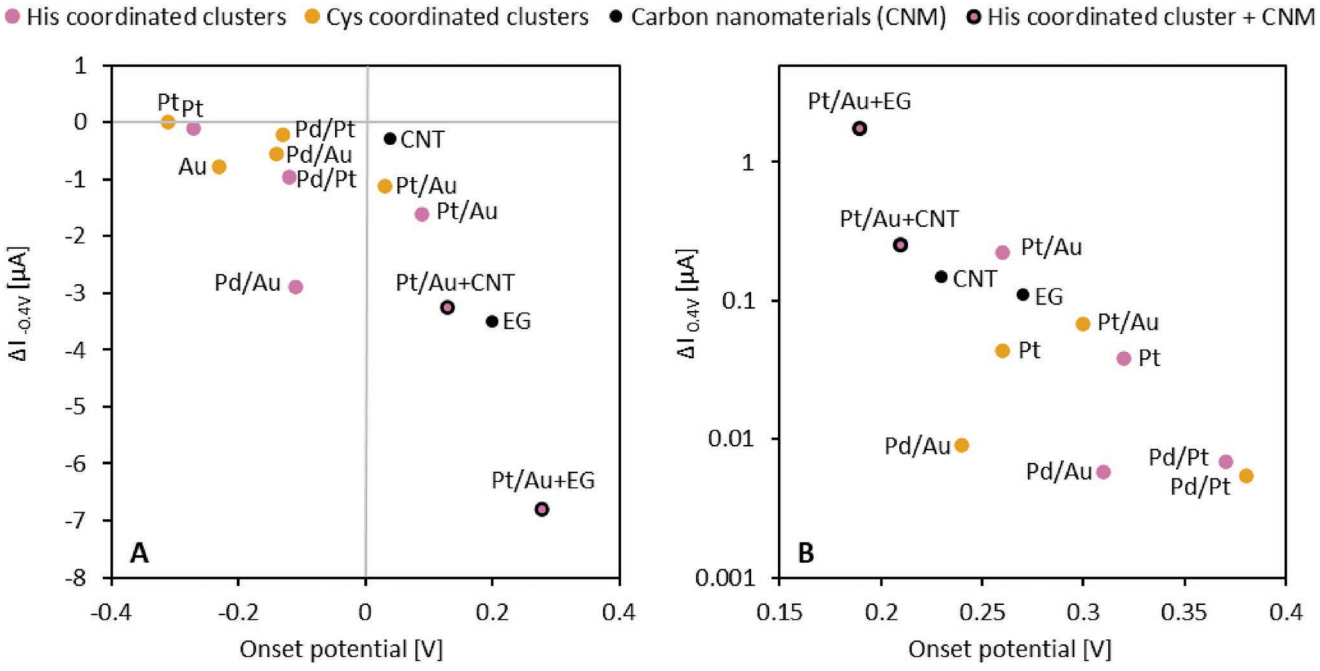

Figure 2. Summary of the electrocatalysts activity, in terms of onset potential and generated current, for the reactions of H_2O_2 A) reduction and B) oxidation. The electrocatalytic materials are categorized based on the chemical composition and nanocluster coordination chemistry.

electrocatalytic activity of the clusters was evaluated in terms of onset potential and faradaic current generated in presence of H_2O_2 (Figure S4, Supporting Information). The onset potential is defined as the potential at which the measured current deviates from the background signal,[54] and represents the energy required by the system to start the electrochemical reaction. Another important parameter to consider is the current generated by the electroactive system, which, for the same WE area, is correlated to the reaction rate and the efficiency of the electron transfer through the material. The faradaic currents were measured at the selected potential values of –0.4 and +0.4 V for H_2O_2 electrochemical reduction and oxidation respectively. At these potentials, the electrochemical reactions were initiated for all the NCs compositions.

Figure 2 summarizes the electrocatalytic behavior of all the synthesized NCs. The most desirable features in the case of the H_2O_2 electrochemical reduction are the strongest negative current and the less negative onset potential (Figure 2A). Generally, histidine-coordinated NCs show stronger currents and higher onset potentials if compared with their cysteine-coordinated counterparts, demonstrating to be better electrocatalysts for H_2O_2 reduction reaction. This could be explained by the fact that sulfur compounds are well-known poisons for precious metal catalysts due to their ability to chemically bond to the catalyst's active site.[55] Catalyst poisoning can operate through four concurrent mechanisms;[56] i) it can decrease the number of active sites, ii) it can modify the chemical nature of the active site so that the catalyst performance is definitively altered, iii) it may change the absorptivity of other species on the neighboring free active sites through an electronic effect, iv) it can alter the average distance that a molecule must diffuse before undergoing reaction on the catalyst surface. The last mechanism is predominant when a poisoning shell is formed at the entrance of the pore of the catalyst or around the catalyst itself, as could be in our case where a macromolecule is used to template the cluster. In this case, the rate of the catalytic reaction may be limited by the rate of diffusion of the reactant toward the reactive sites,[57] resulting in lower faradaic currents generated in presence of H_2O_2.

This trend is not so obvious in the case of the H_2O_2 oxidation reaction (Figure 2B). We believe that in this case, the difference among the cysteine and histidine coordinated clusters is mitigated due to oxidative desorption of the thiol from the metal surface happening at potentials higher than 0.5 V.[58]

Bimetallic clusters, on the other hand, behave better for H_2O_2 reduction compared to monometallic ones. It is reported that, in bimetallic clusters, the interface between two metals provides a bridge for electron transportation, modifying the surface environment of the metals and creating electron-rich and electron-poor zones. This charge depletion can favor the adsorption and desorption strengths of the reagent, providing the optimal environment for electrocatalysis.[59]

Among all the compositions, PtAuNC@$C6_{His16}$ presents the greatest onset potential for H_2O_2 reduction (0.09 V) and as well as a large negative current (–1.61 μA), standing out by far as the best electrocatalyst candidate (Figure 2A). Regarding the H_2O_2 oxidation reaction, we look for the lowest onset potential and maximum current (Figure 2B). Once again, the clusters that better answer these requirements are PtAuNC@$C6_{His16}$ (0.26 V, 0.22 μA), demonstrating to be a versatile catalyst for both H_2O_2 oxidation and reduction.

To better understand the pronounced electrocatalytic properties of PtAuNC@$C6_{His16}$, we further characterized their dimensions and metallic composition by TEM, ICP-MS, and X-ray Photoelectron Spectroscopy (XPS). In **Figure 3**A the

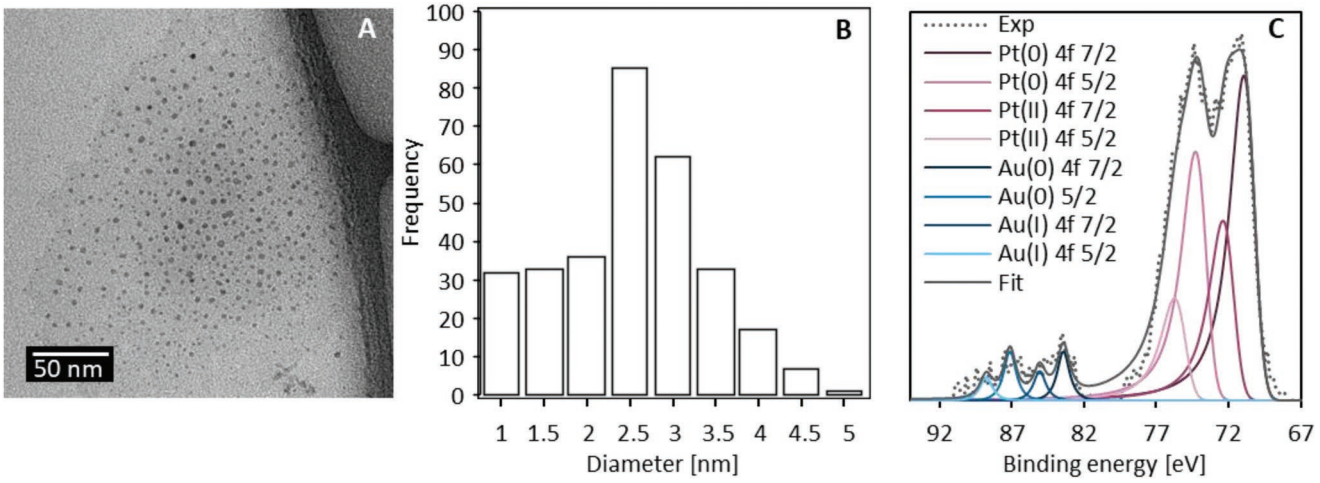

Figure 3. PtAuNC@$C6_{His16}$ characterization: A) TEM micrograph, B) diameter distribution obtained by TEM micrographs, C) deconvoluted high-resolution XPS spectra of the Au 4f (blue solid lines) and Pt 4f (pink solid lines) cores. The dotted lines correspond to the experimental data, the black solid line corresponds to the fitting.

TEM micrograph of PtAuNC@$C6_{His16}$ shows the spherical shape and narrow particle dimensional distribution, centered at 2.59 ± 0.88 nm (Figure 3B). The ratio between Pt and Au was determined to be 6.92 through ICP-MS measurements. The number of metal atoms per C6 unit was calculated from the ratio between the metals and protein concentrations, obtained by BCA colorimetric assay; 50.55 ± 0.58 atoms of Pt and 7.30 ± 0.06 of Au are present for each C6 unit (Table S1, Supporting Information). The valence states of the metals in the NCs were investigated using XPS (Table S2 and Figure S5, Supporting Information). Figure 3C reports the high-resolution spectra of Pt 4f and Au 4f cores. The deconvolution of the Pt signal revealed a mixture of Pt (0) and Pt (II), each one presenting two peaks due to the 4f 5/2 and 4f 7/2 spin splitting. Analogously, the deconvolution of the Au 4f signal showed a mixture of Au (0) and Au (I). Once again, the peaks are split due to the Au 4f 5/2 and Au 4f 7/2 electron spins. The binding energy registered for Pt 4f 7/2 and Au 4f 7/2 bands at the 0-valence state are equal to 70.5 and 83.5 eV respectively. These values are lower if compared to the tabulated values for Pt (0) and Au (0), usually found at 71.1 and 84 eV respectively. This shift has been documented to be a distinctive feature of Pt-Au nanoalloys,[60,61] confirming that the PtAuNC@$C6_{His16}$ are actual metallic alloys and not nanoparticles of segregated metals. Furthermore, we determined that the ratio between Pt (II) and Pt (0) is equal to 0.55, and the corresponding ratio between Au (I) and Au (0) is 0.60. Considering that 0-valence state metals are expected to be in the core of the nanocluster, while the oxidized ones are on the particle surface, the two similar ratios testify that the metals are homogeneously spread in the core and on the surface of the cluster, and that the particles have not a core-shell structure. Finally, these ratios are close to the theoretical values expected for 2.5 nm metal nanoclusters.[62]

With the aim of decreasing the amount of noble metal used in the electroactive material, and therefore the costs of the final ink, we coupled the selected PtAuNC@$C6_{His16}$ with exfoliated graphene (EG) or carbon nanotubes (CNT). These two carbon-based nanomaterials are known to have intrinsic electrocatalytic properties, which can be improved when mixed with metallic nanostructures.[63,64] Furthermore, EG and CNTs are promising candidates for the development of conductive inks and, due to their fascinating physicochemical properties, are becoming increasingly attractive for inkjet printing of low-cost and flexible sensors.[65,66]

Therefore, we investigated if an advantageous effect could originate by using these carbon-based materials and the selected PtAuNC@$C6_{His16}$ together. Both EG and CNTs presented an intrinsic electrocatalytic effect towards both the reduction and oxidation of H_2O_2 (Figures S6 and S7, Supporting Information) and they also showed improved electrochemical properties when physically mixed with the PtAuNC@$C6_{His16}$ in a 1:1 ratio (Figures 2 and 4). However, the effect of EG is more prominent, as it induces a marked shift of the onset potential of 0.21 V towards more positive values when exploited for the electrochemical reduction of H_2O_2, which is combined with a 4-fold increase of current values involved compared to the sole NCs (Figure 4A and Figure S8, Supporting Information). As to the electrochemical oxidation process, the use of the composite material can reduce the onset to +0.07 V while increasing the current 8 folds (Figure 4B and Figure S9, Supporting Information). Different ratios of EG:PtAuNC@$C6_{His16}$ were tested (namely 1:1, 1:2, and 2:1). Modulating the ratio of the two materials did not provide any significative advantage in terms of electrocatalytic properties (Figure S10, Supporting Information). Therefore, 1:1 was chosen as a ratio to perform the following experiments as it is allowed to form stable and homogeneous thin films, avoiding using an excess of precious metals nanoclusters.

To get further insights into the marked electrocatalytic properties of the materials, the dynamics of electron transfer in PtAuNC@$C6_{His16}$ films, EG, and the hybrid film were investigated by means of electrochemical impedance spectroscopy (EIS). EIS was registered at the open circuit potential (OCP) in a PBS solution (pH = 7.0) containing 1 mM $[Fe(CN)_6]^{3-/4-}$ (Figure S11, Supporting Information). The Nyquist plot of EG, at high frequencies, presents a semicircle, representative of a

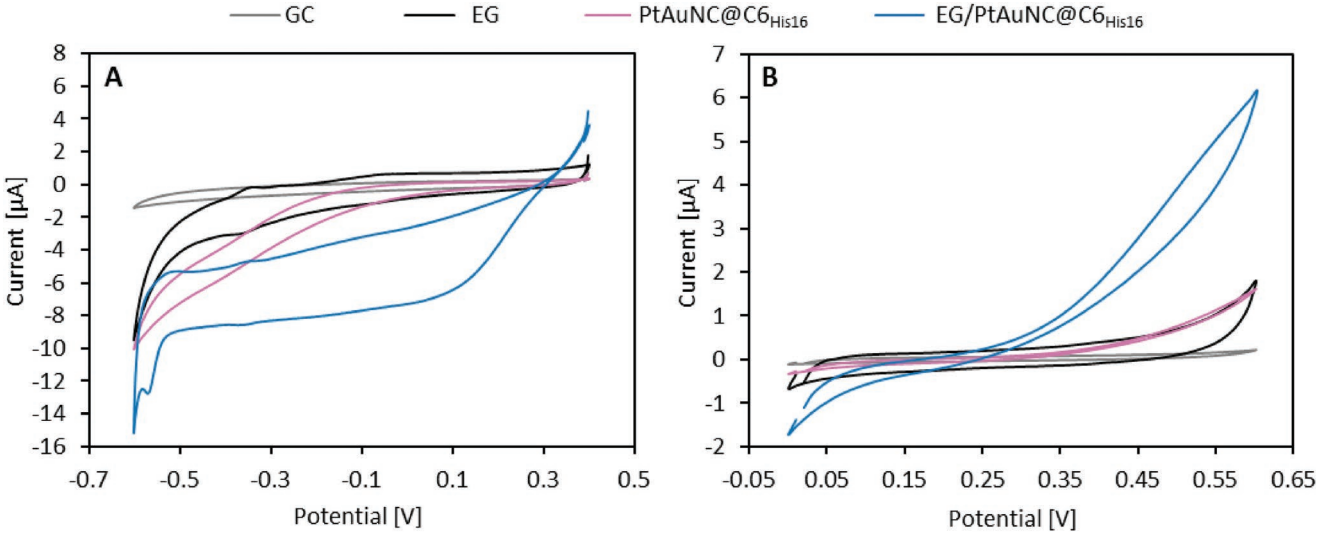

Figure 4. CVs responses registered with naked GC electrode (gray), EG (black), PtAuNC@$C6_{His16}$ (magenta), and a 1:1 mixture of EG and PtAuNC@$C6_{His16}$ (blue), showing the faradaic A) cathodic and B) anodic currents generated in presence of 1 mM H_2O_2.

Faradaic charge transfer process generated by the redox reaction of $[Fe(CN)_6]^{3-/4-}$. The small diameter of the semicircle indicates a low resistance to the charge transfer (1.69 kΩ) as expected for a conductive material such as graphene.[67] At low frequencies, the capacitive behavior of EG predominates, as testified by the vertical tail in the Nyquist plot.[67] A charge transfer process is visible also for PtAuNC@$C6_{His16}$. However, due to the large resistance of the material (1,74 MΩ), the semicircle is not closing, indicating that the protein film hinders the transfer of the electrons. When adding EG, the resistance to the electron transfer diminishes drastically (684 kΩ), testifying to the fundamental role that this material plays in the electron transfer chain.

A further explanation for the higher performances of EG/PtAuNC@$C6_{His16}$ can be found in its electroactive area. By registering CV measurements of Fc-COOH at different scan rates and applying the Randles–Sevcik equation, we calculated and compared the electroactive area of the PtAuNC@$C6_{His16}$ and EG/PtAuNC@$C6_{His16}$ (Figure S12, Supporting Information). Due to the presence of EG, the hybrid film has an electroactive area 4.7 times wider compared to the pure PtAuNC@$C6_{His16}$ film. Therefore, we proved that EG plays a major role, in facilitating the interaction of a higher amount of H_2O_2 with the surface and, at the same time, enhancing the electron-transfer kinetics during its electrocatalytic reactions. Furthermore, it must be considered that the electrocatalytic reduction and oxidation of H_2O_2 follow the same mechanism at the interface of both Pt and graphene,[68–70] therefore, a mechanistic synergism between the two materials cannot be excluded. However, mechanistic analysis of H_2O_2 electrochemistry at the interface of hybrid materials is complex and its details are beyond the scope of the present work.

EG/PtAuNC@$C6_{His16}$ was chosen as the best-performing electroactive material to be used for the ink formulation (Raman, XPS, and TEM characterization of graphene used in this work are reported in Figure S13, Supporting Information). The stability of the material in the investigated electrochemical window was established by registering four consecutive CV traces, without any significative difference among the cycles (Figure S14, Supporting Information).

2.2. Formulation of the Inkjet-Printable Water-Based Electroactive Ink

The lack of manufacturability is the main barrier impeding the translation of new sensing technologies to the market. We plan to overcome this hurdle by formulating an inkjet-printable ink of the above-mentioned electroactive material, with the final aim of producing low-cost amperometric biosensors in a simple, highly repeatable, and scalable fashion.

When formulating an inkjet-printable ink, there are some crucial factors to consider. In the first instance, the ink surface tension and viscosity should be in the "good printability range" defined by the inverse Ohnesorge number (**Equation (1)**).[71,72]

$$Z = \frac{\sqrt{\gamma \rho \alpha}}{\eta} \tag{1}$$

In Equation (1), γ represents the surface tension, ρ the density, α the diameter of the nozzle, and η the viscosity of the ink. When Z is between 1 and 14, the ink creates stable drops. Indeed, low surface tension can promote the Marangoni flow inside the deposited drop of ink, avoiding the coffee-ring effect and, therefore, enhancing the evenness of the printed traces.[73] Instead, viscous inks are less prone to form satellite drops, which are responsible for the loss of the lateral definition and precision of the print.[74] In this work, we aimed to formulate a water-based ink for three reasons: i) to reduce the environmental impact of the ink; ii) to maintain low production costs; and above all iii) to ensure compatibility with the proteins contained in the bio-ink. For these reasons, we chose phosphate-buffered saline (PBS) at pH 7.0 as the base for all our formulations. Nevertheless, the Z value of water is far

from the optimal printable range (equal to 120 for $\alpha = 20$ µm), therefore, co-solvents are required to tune the rheological properties of the ink. We added t-butanol (5% v/v) to decrease the surface tension (Figure S15, Supporting Information) and propylene glycol (5% v/v) to enhance the viscosity (Figure S16, Supporting Information). After the addition of co-solvents, the Z value falls to 12.8, below the maximum recommended value, which predicts good printability. The fast ink absorption and drying dynamics are the other two fundamental parameters determining the efficiency of the printing process. We studied these parameters using partially hydrophobic paper (treated with a 1% polystyrene solution) as a substrate. We selected this printing substrate as it provides an excellent compromise between porosity, permeability, and printing definition. In fact, the pretreatment of paper with hydrophobic polymers is an effective strategy to improve the definition of the printing process.[75] Thanks to the presence of t-butanol, a drop of ink in contact with the partially hydrophobic paper creates an angle of 34.97 ± 1.57°, much lower if compared to the angle formed by the active material in PBS (129.85 ± 0.76°, Figure S17, Supporting Information). Furthermore, while the electroactive material in a PBS solution takes several minutes to be absorbed in the substrate, the drop of ink soaks into the paper in less than a second, facilitating the fast drying of the ink. Upon ink drying, microscopic pictures of the drops were registered confirming the role of the co-solvent in preventing the coffee ring formation (Figure S18, Supporting Information). Finally, we evaluated the colloidal stability of the ink by measuring its sedimentation rate through UV–vis spectroscopy (Figure S19, Supporting Information). The addition of the co-solvents, due to the higher viscosity of the final formulation, increased the colloidal stability of the ink.

2.3. Self-Assembly of the Electroactive Ink

CTPR protein has the unique property to self-assemble upon drying, creating stable and ordered films.[76,77] This property, arising from side-to-side and head-to-tail supramolecular interactions among CTPR units, allows the above-described ink to self-assemble into an electroactive thin film. **Figure 5**A,B show the SEM micrographs of the top view and the cross-section of a film formed by an ink composed of the sole PtAuNC@$C6_{His16}$.

From the top view, it is possible to appreciate the smoothness and the uniformity of the proteinaceous film, while the cross-section depicts the self-standing ordered protein network, accordingly with previous works[78] PtAuNC@$C6_{His16}$ preserve their self-assembly properties when mixed with EG in 1:1 w/w ratio, being able to occlude the carbon nanomaterial into its structure. In Figure 5C,D, the top and the cross-section views of the biofilm formed with the EG/PtAuNC@$C6_{His16}$ bio-ink are reported. The wrinkled structure of EG emerges from the film surface increasing the roughness of the film. The cross-section confirms that the self-standing properties are preserved. Furthermore, the EDX spectrum confirms the presence of Pt in the film (Figure 5E), and the SEM-EDX map shows a homogeneous distribution of the metal in the film (Figure 5F).

It was not possible to verify the presence of Au and map its distribution through SEM-EDX due to the lower amount of this metal in the cluster and the partial overlap with the Pt energies. However, with XPS measurements, we proved that the clusters are alloys of Au and Pt. Therefore, we expect a co-localization of the two metals. Finally, to verify that the presence of the co-solvents does not affect the self-assembly process, we prepared films in the presence and absence of t-butanol and propylene glycol. No adverse effect on the film morphology can

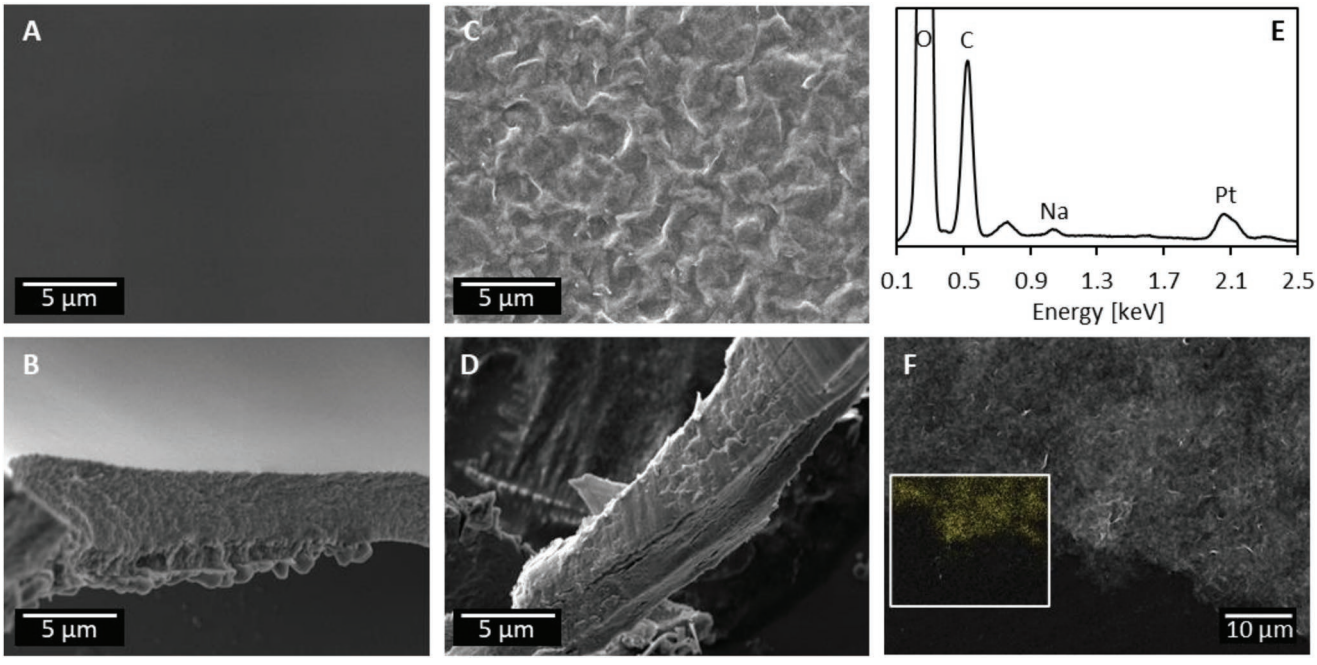

Figure 5. SEM micrographs of the A) top view and B) cross-section of self-assembled PtAuNC@$C6_{His16}$ film. SEM micrographs of the C) top view and D) cross-section of EG/ PtAuNC@$C6_{His16}$ film. E) EDX spectrum and F) Pt map of study of the protein EG/ PtAuNC@$C6_{His16}$ film.

be noticed through SEM micrographs (Figure S20, Supporting Information).

2.4. Inkjet-Printing of the Paper Analytical Devices

ePADs, with a three-electrode configuration cell, were inkjet-printed using a multiple-head 3D bioprinter, with a dedicated head for inkjet printing (**Figure 6**A and Video S1, Supporting Information). The ink was dispensed by means of air pressure and a piezoelectric valve. We used partially hydrophobic filter paper as a substrate, to ensure the permeability of the ink while preserving the printing definition.[75] The traces of the electrode were printed using an ink composed of commercial graphite, suspended in a mixture of water (80% v/v), t-butanol (10% v/v), and propylene glycol (10% v/v). Two passes were required to achieve sufficient conductivity to guarantee the electrode functionality. The resistance of the traces was measured by means of a 4-point probe and resulted in 156.0 ± 13.1 Ω sq^{-1}. The contacts and the pseudo-reference electrode were printed using commercial water-based silver ink (one pass). After the complete hydrophobization of the paper, achieved by soaking it in a solution of 10% polystyrene, the working electrode was modified by inkjet printing using the above-described electroactive bio-ink (one pass). The surfaces of the WE, CE, and RE were investigated through SEM (Figure 6). In all three electrodes,

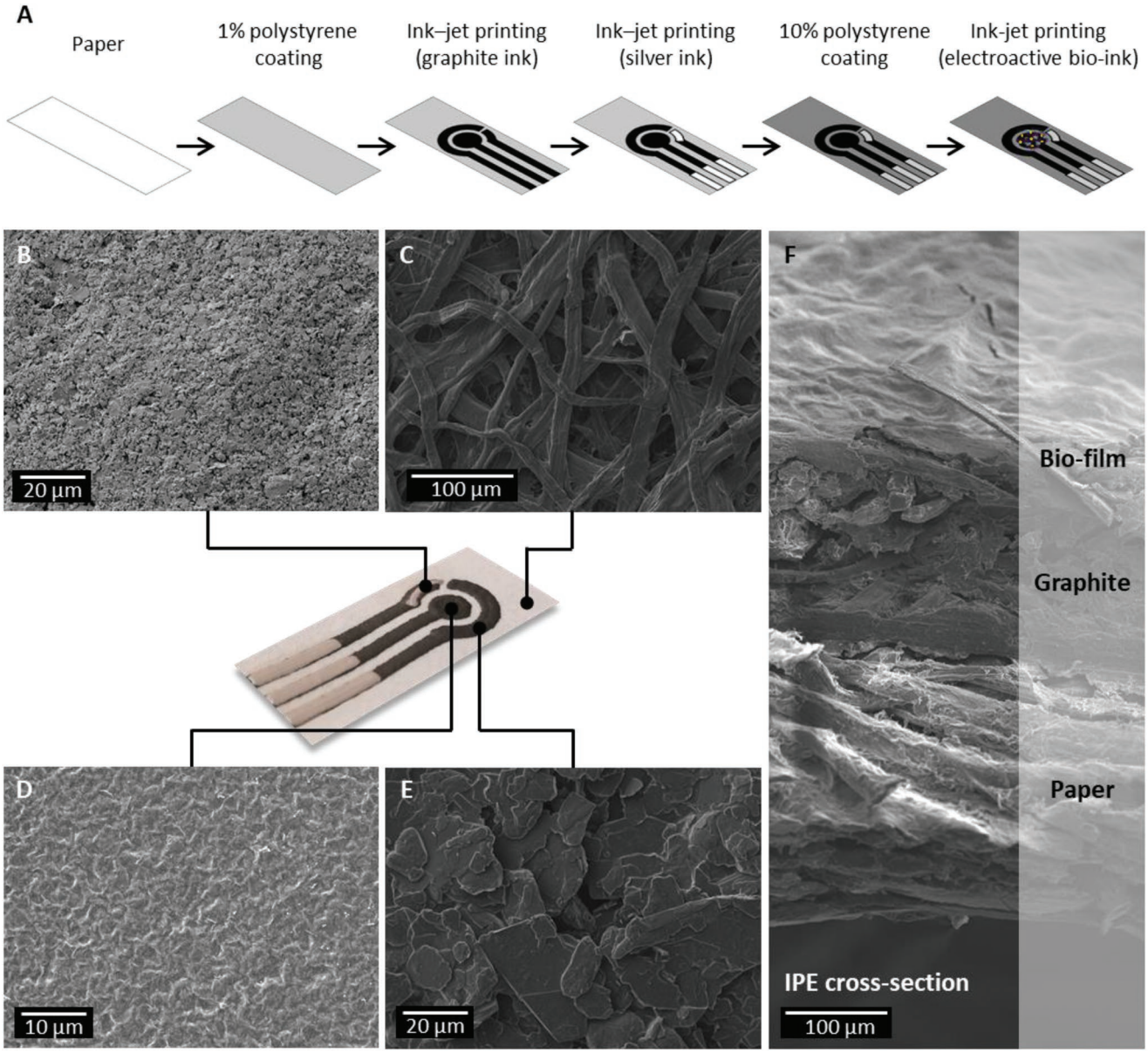

Figure 6. A) Scheme of the inkjet-printing manufacturing process of IPEs. SEM micrographs of the B) Ag RE, and C) paper substrate. Electroactive biofilm on the D) WE, E) graphite CE, and F) cross-section of the WE, where paper, graphite, and electroactive bio-ink can be seen from the bottom to the top.

a homogeneous deposition was achieved completely covering the morphological features of the paper. The SEM micrograph of the WE cross-section shows the layered morphology of the inkjet-printed electrode (IPE)

To understand if the newly developed IPEs could be used as effective ePADs, we performed preliminary electrochemical tests in the absence and presence of an electrochemical probe undergoing redox reversible charge transfer processes, namely ferrocene carboxylic acid (Fc-COOH). The CV showed a difference between Fc-COOH oxidation and reduction potentials of 80 mV (Figure S21A, Supporting Information). The intensity of the oxidation peak is linearly correlated with the square root of the potential scan rate according to the Randles–Sevcik equation and the ratio between the anodic and the cathodic peak heights is close to 1 (Figure S21B, Supporting Information). In conclusion, the manufactured IPEs behave as metal- or carbon-based electrodes commonly used as sensor platforms so they can be therefore used as electrochemical platforms for analytical applications.[79]

We calculated the electrochemical area of the IPE from the CV measurements of Fc-COOH at different scan rates, applying the Randles–Sevcik equation. For IPEs, the electroactive area is 1.2 times larger than the geometrical one, while for commercial carbon screen printed electrodes (C-SPE) this ratio is close to 0.7.[79] In fact, C-SPE contains insulating agents which are added to the ink formulation to make the material processable through screen-printing, improving the mechanical stability of the electrodes but also reducing their electroactive area.[79] This is confirmed by the lower capacitive current presented from the IPEs when compared with the commercial carbon-based SPE (Figure S22, Supporting Information).

2.5. Electrochemical Performances of the PADs

2.5.1. Detection of H_2O_2

To evaluate the electrochemical response of IPEs to changes in H_2O_2 concentration, CV was recorded in PBS, in the absence (blank) and in the presence of 1 mM of the analyte, by depositing a drop of solution on top of the electrode (**Figure 7**A).

The oxidation and reduction peaks of H_2O_2 were both analyzed. In presence of the analyte, an intense anodic current, starting at +0.2 V, was recorded (Figure 7B), while only a low cathodic current intensity was observed (Figure S23, Supporting Information). Therefore, we chose to develop our amperometric biosensor exploiting the anodic peak due to H_2O_2 oxidation and to use +0.4 V as the potential for chronoamperometric measurements, which were used to evaluate the concentration-dependent response of the ink. Ten solutions at different

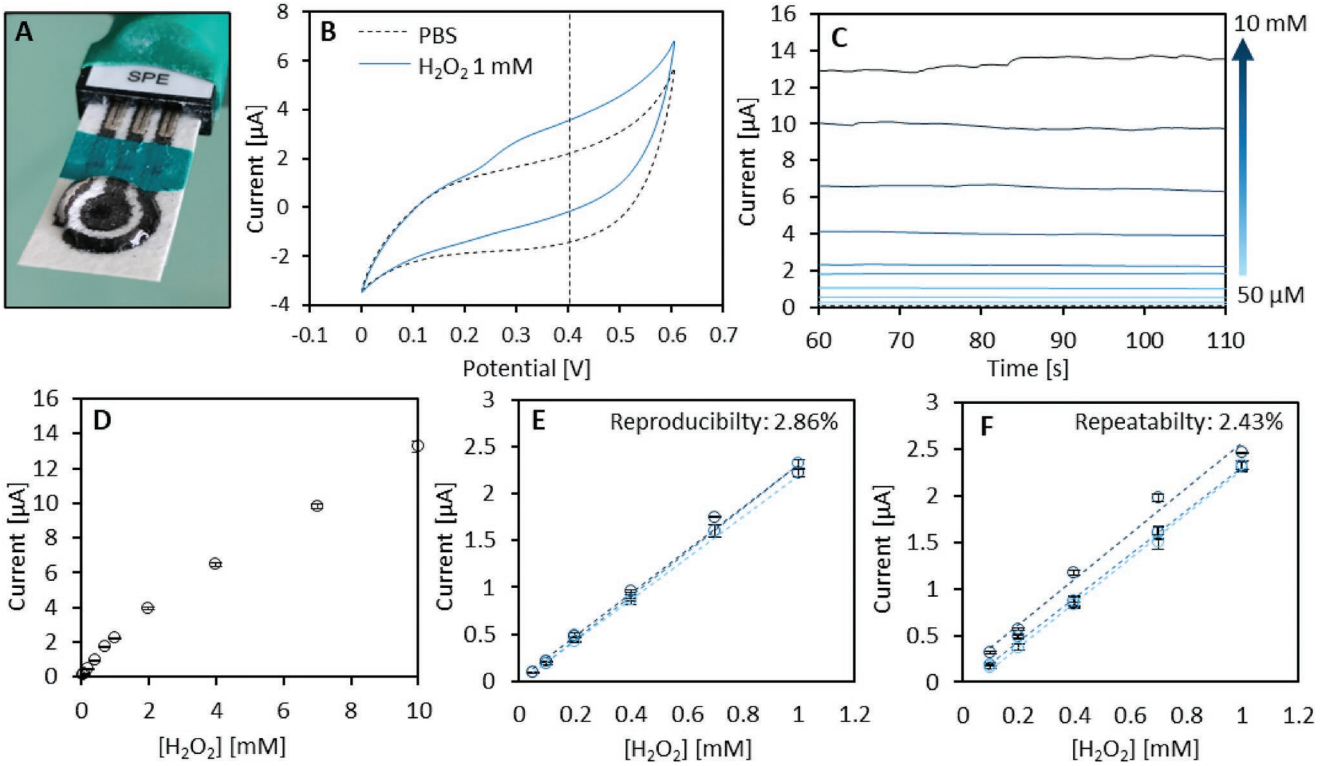

Figure 7. Electrochemical sensing of H_2O_2 in PBS at different concentration levels. A) Picture of the operating IPE. B) CV responses obtained with the IPE, in the absence (dashed line) and presence (solid line) of 1 mM of H_2O_2 (scan rate 20 mV s^{-1}). C) Chronoamperometric response obtained from IPE at 10 different H_2O_2 concentrations namely 0.05, 0.1, 0.2, 0.4, 0.7, 1, 2, 4, 7, and 10 mM (E = +0,4 V). D) Trend of the current measured in CA versus H_2O_2 concentrations. The linear regime was found between 0.05 and 1 mM. E) Calibration lines obtained from three different IPEs. The reproducibility RSD% calculated among the three slopes of the linear calibrations was 2.86%. F) Calibration lines obtained from three consecutive CA calibrations on the same IPE. The repeatability RSD% calculated among the three slopes of the linear calibrations was 2.43%. Error bars represent the standard deviation during 50 s of measurement.

Table 1. Comparison between the sensing performances IPE and commercial C-SPE.

Electrode type	LOD [μM]	Sensitivity [μA mM^{-1} cm^{-2}]	Linear range [mM]	Reproducibility [%]	Repeatability [%]
IPE	0.6 ± 0.2	32.30 ± 0.92	0.05–1.00	2.43	2.86
C-SPE	24.0 ± 2.1	7.87 ± 0.58	0.1–10.0	10.63	7.58

concentrations of H_2O_2 (from 0.05 to 10 mM) were tested under similar conditions (Figure 7C). The current value finally reported is the average of the current values recorded in the last 50 s of the chronoamperometric responses. The response is characterized by a low noise level (8.3 nA) and elevated signal-to-noise ratio. The device presents a linear response against H_2O_2 concentration, in the range of 0.05–10 mM (Figure 7D). The sensitivity of the system was determined to be 32.30 ± 0.92 μA cm^{-2} $мм^{-1}$, with a limit of detection (LOD) of 0.6 μM, calculated as three times the noise in the absence of analyte divided by the slope of the calibration line. The repeatability of the measurements was evaluated by performing three consecutive calibrations over the same electrode and then comparing the resulting electrode sensitivities (Figure 7E). The calculated relative standard deviation (RSD), equal to 2.86%, is lower compared to commercially available electrodes (**Table 1**). This is proof of the exceptional stability of the electroactive bio-ink and the reusability of the IPEs. Reproducibility was tested by performing calibrations on three different electrodes, from which small variations in the sensitivity were registered, with an RSD as low as 2.43%, which confirms a reliable and reproducible response of the IPEs.

We compared the electrochemical performances of our IPE with the ones of a commercially available C-SPE possessing similar electrode geometry, modified by drop-casting the electroactive ink on top of the WE (Table 1 and Figure S24, Supporting Information). We choose C-SPE as a term of comparison since it is a well-established and highly diffused low-cost platform for amperometric sensing. IPEs' linearity range is narrower compared to the one of C-SPE (from 0.1 to 10 mM) (Table 1). However, in this range, IPEs present higher sensitivity and significantly lower LOD compared with commercial screen-printed electrodes. The values of repeatability and reproducibility are lower with respect to the ones of the commercial platform, stating that the inkjet-printed ePADs are competitive platforms for amperometric sensing with the potential to break into the market in the foreseeable future.

To further analyze the market potential of the proposed IPEs we calculated the production costs of the electrode (Table S3, Supporting Information). The cost for a single ePAD is extremely low (0.11 €) and meets the economic requirements to produce disposable sensors. Furthermore, the suggested manufacturing strategy addresses environmental concerns affecting electronics production, as it uses paper as a biodegradable and biocompatible substrate and water-based and low-metal content inks.

The IPE proposed in this work stands out among the few examples of fully inkjet-printed electrodes for H_2O_2 detection reported in literature fulfilling all the requirements (**Table 2**). Furthermore, the herein-described electroactive ink provides the IPE with outstanding sensing performance, despite the very low amount of metals (Pt and Au compose just 0.08% of the WE, Table S4, Supporting Information). The LOD is the lowest among the ones reported in the literature. Moreover, it possesses an optimal linear range for biological applications and good sensitivity.

2.5.2. Detection of Glucose

CTPR-based thin films have been demonstrated to be efficient immobilization matrices for enzymes. The physical entrapment of these biomolecules in the protein film results in improved thermal stability[39] and extended enzymatic activity over time.[85] We recently demonstrated that the integration of CTPR protein films in the design of enzymatic sensors can extend their lifespan from a few days to more than six months improving the repeatability and reproducibility as well.[85]

Table 2. Comparison among the sensing performance of reported fully inkjet-printed H_2O_2 sensors.

Support	Ink base	Electroactive material	Detection Technique	Potential [V]	Linear range	Sensitivity	LOD [μM]	Ref.
Paper	SDS/ Water	MWCNTs Ag NPs	CV	–0.3	0.001–0.7 мм	–	1	[80]
ITO coated glass	Water	PEDOT: PSS/HRP	CA	–0.1	0.25–1 мм	0.544 μA $мм^{-1}$ cm^{-2}	–	[81]
PVC	Dowanol	Ag NPs	CA	–0.4	0.1–6.8 мм	287 μA $мм^{-1}$ cm^{-2}	5	[82]
PET	SDS	SWCNTs SiO_2 NPs HRP	CA/CV	–0.23	1–3 мм	57 ± 3 μA $мм^{-1}$ cm^{-2}	–	[83]
Flexible polyimide and paper	Terpineol cyclohexanone	Graphene	CA	0.5	0.2–1.1 мм	3.32 μA $мм^{-1}$	–	[84]
Paper	Water t-ButOH Propylene glycol	Graphene PtAuNC@ $C6_{His16}$	CA	0.4	0.05–1 мм	32.30 ± 0.92 μA $мм^{-1}$ cm^{-2}	0.6	This work

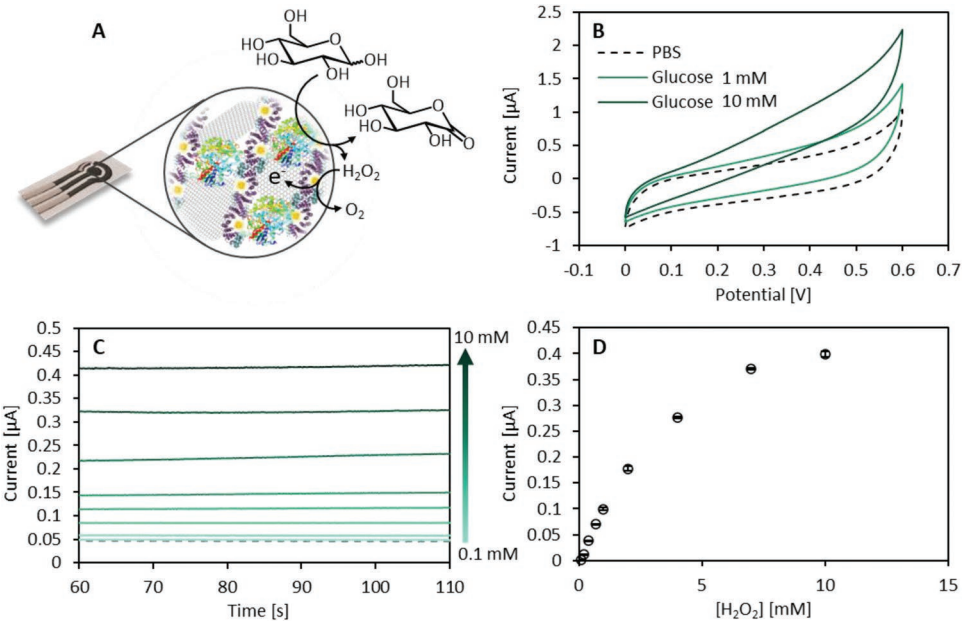

Figure 8. Electrochemical sensing of glucose in PBS at different concentration levels. A) Scheme of the sensing mechanism. B) CV responses obtained with the IPE, in the absence (dashed line) and presence (solid lines) of 1 and 10 mM of glucose (scan rate20 mV s^{-1}). C) Chronoamperometric response obtained from IPE at nine different glucose concentrations, namely 0.1, 0.2, 0.4, 0.7, 1, 2, 4, 7, and 10 mM (E = +0,4 V). D) Trend of the current measured in CA versus H_2O_2 concentrations. The linear regime was found between 0.1 and 1 mM. Error bars represent the standard deviation during 50 s of measurement.

With the aim to exploit this great advantage of CTPR proteins, we introduced glucose oxidase (GOx) in the ink formulation. We exploited this enzymatic bio-ink to fully inkjet-print a glucose biosensor, proving that the application of the presented IPEs can be easily extended to enzymatic biosensing. GOx oxidizes glucose to gluconolactone while producing H_2O_2. In turn, H_2O_2 is transduced into an electron flow by the EG and PtAuNC@$C6_{His16}$ contained in the biofilm, generating a readable signal that is proportional to the glucose concentration in the solution (**Figure 8**A).

The applicability of GOx-IPEs in sensing glucose was investigated by means of electrochemical methods. Figure 8A reports the CV recorded after incubating the GOx-IPE in PBS, in the absence (blank), and in the presence of 1 and 10 mM of the analyte. In presence of the analyte, an anodic current can be registered (Figure 8B), due to the above-described cascade detection mechanism. As was the case with H_2O_2, we polarized the electrode at +0.4 V to perform chronoamperometric detection of glucose. Nine solutions at different concentrations of glucose (from 0.1 to 10 mM) were tested (Figure 8C). The amperometric response, once more, was characterized by extremely low noise (1.1 nA). The sensitivity of the biosensor was 1.67 ± 0.11 µA mM^{-1} cm^{-2}, with a LOD of 17.67 ± 9.02 µM. The GOx-IPEs had a linear response against glucose concentration, in the range of 0.1 to 1 mM (Figure 8D). Both the linear range and sensitivity of the IPEs match the concentrations of glucose expected in sweat (0.02 to 0.6 mM), tears (0.1 to 0.6 mM), and condensed breath (0.4 to 4.0 mM), demonstrating the potential of the developed ink towards quantifying this metabolite in biological fluids.[86] Extended literature research highlighted only two previous examples of fully inkjet-printed ePADs for the detection of glucose,[87,88] both displaying similar analytical performances to the one herein presented (**Table 3**). However, it is worth mentioning that other works on fully inkjet-imprinted electrodes for glucose have been published, using PET or Kepton as substrates.[89,90]

3. Conclusion

Herein, we elucidated the full path that leads to the manufacture of disposable ePADs, from the choice of the electroactive materials, toward the ink formulation, to the inkjet-printing of the electrodes. We investigated, for the first time, the electrocatalytic properties of CTPR-coordinated metallic nanoclusters, demonstrating that these clusters, together with EG can both reduce and oxidize H_2O_2 with extremely low overpotentials and elevated faradaic currents. We formulated a water-based inkjet-printable ink taking into consideration not only the rheological requirements of the manufacturing technique but also the economic and environmental concerns which affect the production of disposable electronics. Finally, we produced ePADs for the detection of H_2O_2 and glucose using this electroactive bio-ink. The sensing performance of the ePADs can compete and, in some aspects, overcome the state of the art of inkjet-printed and commercial screen-printed electrodes, stating the potential of the proposed materials and manufacturing technique. We believe that inkjet printing is currently at the same stage where screen-printing was 20 years ago; at the foot of an uprising curve that could lead it to become a leading technology in sensor manufacturing within a few years. While in this work, we managed to reduce the amount of noble metal required for an effective electrocatalyst, the next works of the group will focus on the use of more abundant and inexpensive metals.

Table 3. Comparison among the sensing performance of reported fully inkjet-printed glucose sensors.

Support	Ink base	Electroactive material	Detection technique	Potential [V]	Linear range	Sensitivity	LOD [μM]	Ref.
Glossy paper	PEDOT/ PSS/ GOPS/ DBSA	Chitosan/ Gox/Fc	CA	0.25	0.025–0.9 mM	–	1	[87]
Photo paper	Water/ Triton X-100	AuNPs	CV	–0.5 0.6	0.05–35 mM	–	10	[88]
Paper	Water t-ButOH Propylene glycol	Graphene PtAuNC@ $C6His_{16}$	CA	0.4	0.1–1 mM	1.67 ± 0.11 μA mM^{-1} cm^{-2}	17.7	This work

4. Experimental Section

Materials and Methods: EG was purchased from SixoniaTech. MW-CNTs were purchased from Nanostructured & Amorphous Materials Inc. and purified by 6 M HCl treatment (12 h) prior to use. GOx (*Aspergillus niger* EU ≥ 100 units mg^{-1}), t-butanol, propylene glycol, polystyrene, Suntronic silver aqueous ink, graphite powder, potassium tetrachloroplatinate, chloroauric acid, and palladium chloride (II) were purchased from Sigma-Aldrich. Sodium-L(+) ascorbate was purchased from VWR Chemicals. Pierce BCA protein assay kit was purchased from Thermo Scientific. Ashless filter paper 589/1 was purchased from Whatman. Commercial reagents and solvents were used as received, without further purification unless otherwise stated. SEM characterization was performed using Zeiss Gemini 500 microscope. For the film formation characterization, solutions of the inks were deposited by drop-casting on top of a SiO substrate, washed with Milli-Q water to remove the excess salts from the film surface, and spattered with conductive metals. For SEM-EDX measurements the film was deposited on top of a highly oriented pyrolytic graphite substrate and imaged without previous sputtering. TEM micrographs were obtained using a JEOL JEM-2100F UHR electron microscope at 200 kV equipped with a TVIPS F-216 CMOS camera and UltimMax 80TSR EDX detector (OXFORD INSTRUMENTS), with 80 mm^2 SDD sensor and 127 eV resolution at 5.9 keV. Samples were prepared by drop-casting 0.4 μL of 10 μM metallic clusters solutions on ultrathin Lacey carbon film-coated Cu-grids (Ted Pella Inc., USA) and drying it under ambient conditions. The image processing and statistics over the electron microscope micrographs were performed with Image J. XPS measurements were carried out using a SPECS SAGE HR 100 spectrometer in high vacuum (10^{-7} Pa), equipped with a nonmonochromatic X-ray Mg source with a Kα line of 1253.6 eV. An electron flood gun was used to neutralize for charging. XPS samples were prepared by drop-casting materials suspensions (1 mg mL^{-1}) on glass slides coated with gold or titanium depending on the sample composition. The spectra were processed and fitted with Casa XPS Version 2.3.16 PR 1.6. Raman spectra were recorded using a Renishaw inVia Raman microscope. A laser excitation wavelength of 532 nm, lens-based spectrometer with 1800 gr mm^{-1} gratings, Peltier-cooled front-illuminated CCD camera (1024 × 532 px), and a 100× objective were employed. Samples were prepared by drop-casting graphene solution on a glass slide and drying it under ambient conditions. Each spectrum is derived from the average of at least 100 spectra recorded in different spots of the sample for 10 s with a laser power of 1.29 mW. Data were processed using Renishaw WiRE 4 software. The absorbance of the ink (0.2 mg mL^{-1}) at 660 nm was monitored through the time by UV–vis spectroscopy (Beckman Coulter DU 800 Spectrophotometer) for 4 h with measurements every 5 min. The relative % absorbance with respect to 0 min was used to evaluate the colloidal stability in time. Rheological properties were characterized using Physica MCR 302 rheometer (Anton Paar). All tests were carried out at 25 °C using a 25 mm parallel plate geometry and a solvent trap to prevent water evaporation. The viscosity of the inks (1.0 mg mL^{-1}) was measured for shear rates from 1 to 1000 s^{-1}, with a gap equal to 1 mm. The viscosity of the ink is independent of the shear rate and has been calculated as average across the measurement range. Pendant drop and contact angle measurements were performed using a DSA100 Kruss contact angle meter dispensing 2.0 μL drops and fitting with Young–Laplace equation. The obtained values were the average of ten measurements. Electrochemical characterizations were performed through CV and CA at constant potential with an electrochemical workstation Autolab MSTAT204 potentiostat/galvanostat (Metrohm). EIS was registered in a three-electrode conformation using PET-ITO electrode modified with the nanomaterials as a WE, Pt mesh as a CE, and Ag/AgCl as a RE. The measurements were performed in PBS solution (pH = 7) containing 1 mM $[Fe(CN)_6]^{3-/4-}$, at the OCP applying a perturbation equal to 10 mV in the frequency range comprised between 100 kHz and 10 mHz. A multi-headed 3D Discovery bioprinter (RegenHU, Switzerland) equipped with an inkjet printing head was employed to print the IPEs. The ink was dispensed by means of air pressure (20 mBar) and a piezoelectric valve (300 μs opening-closure interval). A nozzle with an internal diameter of 100 μm was employed selecting 0.2 mm as the distance between two deposited droplets.

CTPR Protein Expression: CTPR proteins were cloned into pProEx-HTA vector and were expressed in *Escherichia coli* C41 (DE3) strain following a previously reported protocol for affinity purification.[91] After growing the cells in Luria–Bertani media (LB) with ampicillin, the protein expression was inducted by 1 mM isopropyl β-d-thiogalactopyranoside (IPTG) at an optical density (OD) of 0.6–0.8 and the cells grown for additional 16 h at 20 °C. Lysis buffer (300 mM sodium chloride, 50 mM Tris pH 8.0) was used to resuspend the cell pellets and they were lysed by sonication. CTPR proteins were purified via affinity chromatography using Ni-NTA resin. The tobacco etch virus (TEV) protease was used to cleave the N-terminal hexahistidine tag from the proteins. Finally, a second purification was performed to remove the remaining protease and the his-tag from the CTPR protein samples. For cysteine-coordinated proteins, the second purification was performed as described before, and for histidine-coordinated proteins, the final purification was achieved by fast protein liquid chromatography (FPLC), since the cleaved protein would still bind to the Ni-NTA resin. Lastly, electrophoresis gels helped to confirm the accurate molecular weight and the purity of the purified proteins. The protein concentration was measured by UV absorbance at 280 nm, using extinction coefficients at 280 nm calculated from the amino acid composition. The amino acid sequences of both proteins are reported in the Supporting Information.

CTPR-NCs Synthesis: Different compositions of monometallic (gold and platinum) and bimetallic (gold and platinum, gold and palladium, and platinum and palladium) clusters were synthesized as follows (using potassium tetrachloroplatinate, chloroauric acid, and palladium chloride (II) as metal salt precursors). 20 μM of CTPR protein was incubated along with 32 metal salt equivalents for the monometallic compositions. The bimetallic gold and platinum, and gold and palladium clusters were synthesized in a ratio of 1:10, using 32, and 320 metal salt equivalents respectively, while the bimetallic platinum and palladium clusters were synthesized in a ratio of 1:1 with 64 metal salt equivalents. The reactions were incubated at 50 °C and 800 rpm for 30 min. 30-min

incubation was performed to allow the binding of the metal ions to the metal-coordinating sites. Sodium-L-ascorbate was then added, as a reducing agent, according to the metal concentration of each reaction in an excess of 100 times more. The reaction was then incubated for 72 h at 50 °C and 800 rpm. After the incubation, the nanoclusters were centrifuged at 16 000 rpm for 1 h at 4 °C, the supernatant was concentrated using Amicon filters (cut-off 10 kDa) at 4500 rpm and the final product was purified using a PD-10 gel filtration column A. BCA assay was performed to calculate the final protein concentration. The clusters were characterized by TEM, X-ray photoelectron spectroscopy (XPS), and inductively coupled plasma mass spectroscopy (ICP-MS).

Inkjet-Printing of the ePADs: For the manufacturing of the ePADs, Whatman ashless filter paper 589/1 had been used as a substrate. As a first step, a 1% polystyrene solution in toluene was employed to make the substrate partially hydrophobic. The traces of electrodes were printed with graphite ink (80 mg mL^{-1}; water 80%, t-butanol 10%, propylene glycol 10%; 2 passes). Then, the contacts and pseudo-reference electrode were printed using Suntronic silver aqueous ink (100 mg mL^{-1}, 1 pass). Then the ePADs were treated with 10% polystyrene solution in toluene to assure the complete impermeability of the paper. Finally, the electroactive ink was printed (2 mg mL^{-1}, 1 pass).

Electrochemical Measurements: The electrocatalytic properties of the materials were evaluated using a GC electrode (with a diameter of 3 mm, purchased from Metrohm, Spain). For all the characterization experiments, 5 µL of the sample (0.2 mg mL^{-1}) was drop-cast on the GC electrode and left to dry at room temperature. Once dried, 2 µL of a 1% Nafion solution (neutralized at pH 7.0) were drop-cast onto the electrode surface and left to evaporate at room temperature. For the nanocluster characterization towards H_2O_2 reduction, the potential was cycled between –0.6 and +0.4 V in an argon atmosphere (obtained by bubbling argon into the solution for 15 min). For the nanoclusters characterization towards H_2O_2 oxidation, CV experiments were performed between +0.0 and +0.6 V. CVs were repeated four times at a scan rate of 0.02 V s^{-1} in 0.1 M of PBS enriched with 0.1 M of KCl.

The amperometric characterization of the sensor was accomplished using the produced IPEs or comercial C-SPE(DRP-110, purchased from Methrom DropSens, Spain). The latters present a circular working electrode with a 4 mm diameter, a counter electrode made of carbon, and a silver pseudo-reference electrode. Analogously, 10 µL of the material was deposited in the working electrode by drop-casting and 2 µL of Nafion was used to prevent the leakage of the samples. Chronoamperometric experiments were performed by applying a constant potential of +0.4 V for 100 s. The reproducibility was assessed by using three different electrodes to perform a calibration on the same day and the repeatability was evaluated by using the same electrode to perform three consecutive calibrations. Sensitivity was calculated by normalization of the slope in the linear range to the electrode area. The noise was determined as the SD of the amperometric responses in PBS recorded during the last 50 s. LOD was calculated as three times the standard deviation of the measurement in PBS divided by the slope of the calibration line. Each measurement was performed in triplicate.

Supporting Information

Supporting Information is available from the Wiley Online Library or from the author.

Acknowledgements

A.S. and S.V.-D. contributed equally to this work. A.S. acknowledges support by Juan de la Cierva Formacion/no. Grant FJC2018-036777-I, funded by MCIN/AEI/ 10.13039/501100011033). M.P., as the recipient of the AXA Bionanotechnology Chair, is grateful to the AXA Research Fund for financial support. A.L.C. acknowledges support by the Agencia Estatal de Investigación Grant PID2019-111649RB-I00 funded by MCIN/AEI/ 10.13039/501100011033 and support by the Agencia Estatal de Grant PDC2021-120957-I00 funded by MCIN/AEI/ 10.13039/501100011033 and by the "European Union NextGenerationEU/PRTR. This project has received funding from the European Union's Horizon 2020 Research and Innovation Programme under Grant Agreement No. 964593. This project has received funding from the European Union's Horizon 2020 Research and Innovation Programme under Grant Agreement **No**. 964248. This work was performed under the Maria de Maeztu Units of Excellence Program from Q5 the Spanish State Research Agency grant no. MDM-2017-0720.

Conflict of Interest

The authors declare no conflict of interest.

Data Availability Statement

The data that support the findings of this study are available in the supplementary material of this article.

Keywords

biosensors, electrocatalysis, electrochemical paper-based analytical devices, engineered proteins, graphene, inkjet printing, water-based inks

Received: January 6, 2023
Revised: March 11, 2023
Published online:

[1] C. Dincer, R. Bruch, E. Costa-Rama, M. T. Fernández-Abedul, A. Merkoçi, A. Manz, G. A. Urban, F. Güder, *Adv. Mater.* **2019**, *31*, 5531.
[2] M. Tan, C. Owh, P. L. Chee, A. Kyaw, D. Kai, X. J. Loh, *J. Mater. Chem. C* **2016**, *4*, 5531
[3] M. Irimia-Vladu, E. D. Głowacki, G. Voss, S. Bauer, N. S. Sariciftci, *Mater. Today* **2012**, *15*, 340.
[4] A. Moya, G. Gabriel, R. Villa, F. Javier del Campo, *Curr. Opin. Electrochem.* **2017**, *3*, 29.
[5] Y. Khan, A. Thielens, S. Muin, J. Ting, C. Baumbauer, A. C. Arias, *Adv. Mater.* **2020**, *32*, 1905279.
[6] M. Zea, A. Moya, R. Villa, G. Gabriel, *Adv. Mater. Interfaces* **2022**, *9*, 2200371.
[7] F. Arduini, *Curr. Opin. Electrochem.* **2022**, *35*, 101090.
[8] A. Koutsioukis, V. Belessi, V. Georgakilas, *Green Chem.* **2021**, *23*, 5442.
[9] P. G. Karagiannidis, S. A. Hodge, L. Lombardi, F. Tomarchio, N. Decorde, S. Milana, I. Goykhman, Y. Su, S. v Mesite, D. N. Johnstone, R. K. Leary, P. A. Midgley, N. M. Pugno, F. Torrisi, A. C. Ferrari, *ACS Nano* **2017**, *11*, 2742.
[10] S. F. Kamarudin, M. Jaafar, A. Abd Manaf, Y. Takamura, T. Masuda, Y. Yumoto, *Adv. Mater. Technol.* **2021**, *6*, 2001026.
[11] F. Torrisi, T. Hasan, W. Wu, Z. Sun, A. Lombardo, T. S. Kulmala, G.-W. Hsieh, S. Jung, F. Bonaccorso, P. J. Paul, D. Chu, A. C. Ferrari, *ACS Nano* **2012**, *6*, 2992.
[12] A. Silvestri, A. Criado, F. Poletti, F. Wang, P. Fanjul-Bolado, M. B. González-García, C. García-Astrain, L. M. Liz-Marzán, X. Feng, C. Zanardi, M. Prato, *Adv. Funct. Mater.* **2022**, *32*, 2105028.
[13] D. McManus, S. Vranic, F. Withers, V. Sanchez-Romaguera, M. Macucci, H. Yang, R. Sorrentino, K. Parvez, S.-K. Son, G. Iannaccone, K. Kostarelos, G. Fiori, C. Casiraghi, *Nat. Nanotechnol.* **2017**, *12*, 343.

[14] L.-C. Jia, C.-G. Zhou, W.-J. Sun, L. Xu, D.-X. Yan, Z.-M. Li, *Chem. Eng. J.* **2020**, *384*, 123368.
[15] Y. Liu, B. Derby, *Phys. Fluids* **2019**, *31*, 032004.
[16] H. Hu, R. Larson, *J. Phys. Chem. B* **2006**, *110*, 7090.
[17] L. Setti, A. Fraleoni-Morgera, I. Mencarelli, A. Filippini, B. Ballarin, M. Biase, *Sens. Actuators, B* **2007**, *126*, 252.
[18] H. Shamkhalichenar, J.-W. Choi, *J. Electrochem. Soc.* **2017**, *164*, B3101.
[19] C. Casiraghi, M. Macucci, K. Parvez, R. Worsley, Y. Shin, F. Bronte, G. Fiori, *Carbon* **2017**, *129*, 462.
[20] H. Ling, R. Chen, Q. Huang, F. Shen, Y. Wang, X. Wang, *Green Chem.* **2020**, *22*, 3208.
[21] T. Kant, K. Shrivas, K. Dewangan, A. Kumar, N. K. Jaiswal, M. K. Deb, S. Pervez, *Mater. Today Chem.* **2022**, *24*, 100769.
[22] P. Wang, B. Barnes, Z. Huang, Z. Wang, M. Zheng, Y. Wang, *Adv. Mater.* **2021**, *33*, 2005890.
[23] M. Franco, R. Alves, N. Perinka, C. Tubio, P. Costa, S. Lanceros-Mendéz, *ACS Appl. Electron. Mater.* **2020**, *2*, 2857.
[24] Y. Wang, S. Peng, S. Zhu, Y. Wang, Z. Qiang, C. Ye, Y. Liao, M. Zhu, *ACS Appl. Mater. Interfaces* **2021**, *13*, 57930.
[25] Q. Duan, B. Lan, Y. Lv, *ACS Appl. Mater. Interfaces* **2022**, *14*, 1973.
[26] X. Gong, L. Zhang, Y. Huang, S. Wang, G. Pan, L. Li, *RSC Adv.* **2020**, *10*, 22222.
[27] S. Li, A. Kosek, M. N. Jahangir, R. Malhotra, C.-H. Chang, *Adv. Funct. Mater.* **2021**, *31*, 2006273.
[28] J. S. Austin, N. D. Cottam, C. Zhang, F. Wang, J. H. Gosling, O. Nelson-Dummet, T. S. S. James, P. H. Beton, G. F. Trindade, Y. Zhou, C. J. Tuck, R. Hague, O. Makarovsky, L. Turyanska, *Nanoscale* **2023**, *15*, 2134.
[29] R. F. Hossain, I. G. Deaguero, T. Boland, A. B. Kaul, *npj 2D Mater. Appl.* **2017**, *1*, 28.
[30] G. Barandun, L. Gonzalez-Macia, H. S. Lee, C. Dincer, F. Güder, *ACS Sens.* **2022**, *7*, 2804.
[31] O. Ogbeide, G. Bae, W. Yu, E. Morrin, Y. Song, W. Song, Y. Li, B.-L. Su, K.-S. An, T. Hasan, *Adv. Funct. Mater.* **2022**, *32*, 2113348.
[32] Y. Shen, S. Hou, D. Hao, X. Zhang, Y. Lu, G. Zu, J. Huang, *ACS Appl. Electron. Mater.* **2021**, *3*, 4081.
[33] E. Bilbao, S. Kapadia, V. Riechert, J. Amalvy, F. N. Molinari, M. M. Escobar, R. R. Baumann, L. N. Monsalve, *Sens. Actuators, B* **2021**, *346*, 130558.
[34] P. He, J. R. Brent, H. Ding, J. Yang, D. J. Lewis, P. O'Brien, B. Derby, *Nanoscale* **2018**, *10*, 5599.
[35] T. Kajander, A. Cortajarena, S. Mochrie, L. Regan, *Acta Crystallogr., Sect. D: Biol. Crystallogr.* **2007**, *63*, 800.
[36] D. Sánchez de Alcázar, D. Romera, J. Castro-Smirnov, A. Sousaraei, S. Casado, A. Espasa, M. Morant-Miñana, J. J. Hernandez, I. Rodriguez, R. Costa, J. Cabanillas-Gonzalez, R. Martinez, A. Cortajarena, *Nanoscale Adv.* **2019**, *1*, 3980.
[37] T. Grove, L. Regan, A. Cortajarena, *J. R. Soc., Interface* **2013**, *10*, 20130051.
[38] S. Mejias, E. López-Martínez, M. Fernandez, P. Couleaud, A. Martin-Lasanta, D. Romera, A. Sánchez Iglesias, S. Casado, M. Osorio, J. Abad, M. T. González, A. Cortajarena, *Nanoscale* **2021**, *13*, 6772.
[39] D. Sánchez de Alcázar, S. Velasco-Lozano, N. Zeballos, F. López-Gallego, A. Cortajarena, *ChemBioChem* **2019**, *20*, 1977.
[40] A. Silvestri, F. Wang, X. Feng, A. Cortajarena, M. Prato, *J. Mater. Chem. C* **2022**, *10*, 5466.
[41] E. López-Martínez, D. Gianolio, S. Garcia-Orrit, V. Vega-Mayoral, J. Cabanillas-Gonzalez, C. Sanchez-Cano, A. Cortajarena, *Adv. Opt. Mater.* **2021**, *10*, 2101332.
[42] A. Aires, A. Sousaraei, M. Möller, J. Cabanillas-Gonzalez, A. L. Cortajarena, *Nano Lett.* **2021**, *21*, 9347.
[43] A. Aires, I. Llarena, M. Möller, J. Castro-Smirnov, J. Cabanillas-Gonzalez, A. Cortajarena, *Angew. Chem.* **2019**, *131*, 6280.
[44] S. H. Mejias, Z. Bahrami-Dizicheh, M. Liutkus, D. J. Sommer, A. Astashkin, G. Kodis, G. Ghirlanda, A. L. Cortajarena, *Chem. Commun.* **2019**, *55*, 3319.
[45] T. Higaki, Q. Li, M. Zhou, S. Zhao, Y. Li, S. Li, R. Jin, *Acc. Chem. Res.* **2018**, *51*, 2764.
[46] K. Joya, A. Munir, S. Z. Hussain, N. Ullah, A. Qurashi, I. Hussain, N. Babar, *ChemSusChem* **2018**, *12*, 1517.
[47] K. Kwak, D. Lee, *Acc. Chem. Res.* **2019**, *52*, 12.
[48] A. L. Cortajarena, L. Regan, *Protein Sci.* **2011**, *20*, 336.
[49] T. Kajander, A. L. Cortajarena, E. R. G. Main, S. G. J. Mochrie, L. Regan, *J. Am. Chem. Soc.* **2005**, *127*, 10188.
[50] A. Aires, A. Sousaraei, M. Möller, J. Cabanillas-Gonzalez, A. L. Cortajarena, *Nano Lett.* **2021**, *21*, 9347.
[51] S. W. May, *Curr. Opin. Biotechnol.* **1999**, *10*, 370.
[52] T. Finkel, M. Serrano, M. A. Blasco, *Nature* **2007**, *448*, 767.
[53] K. Barnham, C. Masters, A. Bush, *Nat. Rev. Drug Discovery* **2004**, *3*, 205.
[54] A. J. R. Botz, M. Nebel, R. A. Rincón, E. Ventosa, W. Schuhmann, *Electrochim. Acta* **2015**, *179*, 38.
[55] N. S. Nasri, J. M. Jones, V. A. Dupont, A. Williams, *Energy Fuels* **1998**, *12*, 1130.
[56] P. Forzatti, L. Lietti, *Catal. Today* **1999**, *52*, 165.
[57] H. Wise, in *Catalyst Deactivation 1991*, (Eds: C. H. Bartholomew, J. B. Butt) Elsevier, Amsterdam, **1991**, p. 497.
[58] M. W. J. Beulen, M. I. Kastenberg, F. C. J. M. van Veggel, D. N. Reinhoudt, *Langmuir* **1998**, *14*, 7463.
[59] Q. Shao, P. Wang, X. Huang, *Adv. Funct. Mater.* **2019**, *29*, 1806419.
[60] S. Christensen, M. MacDonald, A. Chatt, P. Zhang, H. Qian, R. Jin, *J. Phys. Chem. C* **2012**, *116*, 26932.
[61] B. Mao, L. Qian, G. Maduraiveeran, Z.-G. Liu, A. Chen, *Microchim. Acta* **2021**, *188*, 276.
[62] K. J. Klabunde, J. Stark, O. Koper, C. Mohs, D. G. Park, S. Decker, Y. Jiang, I. Lagadic, D. Zhang, *J. Phys. Chem.* **1996**, *100*, 12142.
[63] S. Guo, D. Wen, Y. Zhai, S. Dong, E. Wang, *ACS Nano* **2010**, *4*, 3959.
[64] C. Rogers, W. S. Perkins, G. Veber, T. E. Williams, R. R. Cloke, F. R. Fischer, *J. Am. Chem. Soc.* **2017**, *139*, 4052.
[65] F. Torrisi, T. Hasan, W. Wu, Z. Sun, A. Lombardo, T. S. Kulmala, G.-W. Hsieh, S. Jung, F. Bonaccorso, P. J. Paul, D. Chu, A. C. Ferrari, *ACS Nano* **2012**, *6*, 2992.
[66] S. F. Kamarudin, M. Jaafar, A. Abd Manaf, Y. Takamura, T. Masuda, Y. Yumoto, *Adv. Mater. Technol.* **2021**, *6*, 2001026.
[67] E. Casero, A. M. Parra-Alfambra, M. D. Petit-Domínguez, F. Pariente, E. Lorenzo, C. Alonso, *Electrochem. Commun.* **2012**, *20*, 63.
[68] I. Katsounaros, W. B. Schneider, J. C. Meier, U. Benedikt, P. U. Biedermann, A. A. Auer, K. J. J. Mayrhofer, *Phys. Chem. Chem. Phys.* **2012**, *14*, 7384.
[69] S. J. Amirfakhri, D. Binny, J.-L. Meunier, D. Berk, *J. Power Sources* **2014**, *257*, 356.
[70] G. L. Luque, M. I. Rojas, G. A. Rivas, E. P. M. Leiva, *Electrochim. Acta* **2010**, *56*, 523.
[71] A. Silvestri, A. Criado, F. Poletti, F. Wang, P. Fanjul-Bolado, M. B. González-García, C. García-Astrain, L. M. Liz-Marzán, X. Feng, C. Zanardi, M. Prato, *Adv. Funct. Mater.* **2022**, *32*, 2105028.
[72] D. McManus, S. Vranic, F. Withers, V. Sanchez-Romaguera, M. Macucci, H. Yang, R. Sorrentino, K. Parvez, S.-K. Son, G. Iannaccone, K. Kostarelos, G. Fiori, C. Casiraghi, *Nat. Nanotechnol.* **2017**, *12*, 343.
[73] H. Hu, R. Larson, *J. Phys. Chem. B* **2006**, *110*, 7090.
[74] Y. Liu, B. Derby, *Phys. Fluids* **2019**, *31*, 032004.
[75] M. Zea, A. Moya, R. Villa, G. Gabriel, *Adv. Mater. Interfaces* **2022**, *9*, 2200371.
[76] T. Grove, L. Regan, A. Cortajarena, *J. R. Soc., Interface* **2013**, *10*, 20130051.

[77] D. Sánchez de Alcázar, D. Romera, J. Castro-Smirnov, A. Sousaraei, S. Casado, A. Espasa, M. Morant-Miñana, J. J. Hernandez, I. Rodriguez, R. Costa, J. Cabanillas-Gonzalez, R. Martinez, A. Cortajarena, *Nanoscale Adv.* **2019**, *1*, 3980.
[78] N. A. Carter, T. Z. Grove, *Biomacromolecules* **2015**, *16*, 706.
[79] F. Poletti, A. Scidà, B. Zanfrognini, A. Kovtun, V. Parkula, L. Favaretto, M. Melucci, V. Palermo, E. Treossi, C. Zanardi, *Adv. Funct. Mater.* **2022**, *32*, 2107941.
[80] H. Shamkhalichenar, J.-W. Choi, *J. Electrochem. Soc.* **2017**, *164*, B3101.
[81] L. Setti, A. Fraleoni-Morgera, I. Mencarelli, A. Filippini, B. Ballarin, M. di Biase, *Sens. Actuators, B* **2007**, *126*, 252.
[82] L. Shi, M. Layani, X. Cai, H. Zhao, S. Magdassi, M. Lan, *Sens. Actuators, B* **2018**, *256*, 938.
[83] M. Mass, L. Veiga, O. Garate, G. Longinotti, A. Moya, E. Ramon, R. Villa, G. Ybarra, G. Gabriel, *Nanomaterials* **2021**, *11*, 1645.
[84] S. R. Das, Q. Nian, A. A. Cargill, J. A. Hondred, S. Ding, M. Saei, G. J. Cheng, J. C. Claussen, *Nanoscale* **2016**, *8*, 15870.
[85] A. Silvestri, F. Wang, X. Feng, A. Cortajarena, M. Prato, *J Mater Chem C Mater* **2022**, *10*, 5466.
[86] E. Witkowska Nery, M. Kundys-Siedlecka, P. Jeleń, M. Jönsson-Niedziolka, *Anal. Chem.* **2016**, *88*, 11271.
[87] E. Bihar, S. Wustoni, A. M. Pappa, K. N. Salama, D. Baran, S. Inal, *npj Flexible Electron.* **2018**, *2*, 30.
[88] T. Kant, K. Shrivas, K. Tapadia, R. Devi, V. Ganesan, M. K. Deb, *New J. Chem.* **2021**, *45*, 8297.
[89] R. Bernasconi, A. Mangogna, L. Magagnin, *J. Electrochem. Soc.* **2018**, *165*, B3176.
[90] T. Pandhi, C. Cornwell, K. Fujimoto, P. Barnes, J. Cox, H. Xiong, P. H. Davis, H. Subbaraman, J. E. Koehne, D. Estrada, *RSC Adv.* **2020**, *10*, 38205.
[91] A. Aires, A. Sousaraei, M. Möller, J. Cabanillas-Gonzalez, A. L. Cortajarena, *Nano Lett.* **2021**, *21*, 9347.